Neuroadaptive Admittance Control for Human–Robot Interaction With Human Motion Intention Estimation and Output Error Constraint

Chengguo Liu[®], Kai Zhao[®], *Member, IEEE*, Weiyong Si[®], *Member, IEEE*, Junyang Li[®], and Chenguang Yang[®], *Fellow, IEEE*

Abstract—Human-robot interaction (HRI) is a crucial component in the field of robotics, and enabling faster response, higher accuracy, as well as smaller human effort, is essential to improve the efficiency, robustness, and applicability of HRI-driven tasks. In this article, we develop a novel neuroadaptive admittance control with human motion intention (HMI) estimation and output error constraint for natural and stable interaction. First, the interaction force information of the robot is utilized to predict the HMI and the stiffness in the admittance model is dynamically updated based on surface electromyography (sEMG) signals of the human upper limb to achieve human-like compliance. Then, based on the designed error transformation mechanism, an innovative prescribed performance control (PPC) is proposed that allows the trajectory error to converge to the given constraint range within a predefined time for any bounded initial conditions, thus enabling the robot to maintain a comprehensive performance of moving in the desired direction as guided by the human. Also, an adaptive neural network (NN) is employed to compensate for the uncertainty of robotics systems to improve the tracking accuracy further. According to the Lyapunov stability analysis criterion, our approach ensures that all states of the closedloop system remain globally uniformly ultimately bounded. Finally, a series of real-world robot experiments demonstrate the effectiveness of the proposed framework.

Index Terms—Adaptive admittance control, human motion intention (HMI) estimation, human-robot interaction (HRI), neural network (NN), output error constraint.

Received 21 January 2025; revised 20 March 2025; accepted 23 March 2025. This work was supported in part by the National Natural Science Foundation of China under Grant 52375041, and Grant 62403082; in part by the Chongqing Top-Notch Young Talents Project under Grant cstc2024ycjhbgzxm0085; and in part by the Fundamental Research Funds for the Central Universities under Grant 2023CDJKYJH091. This article was recommended by Associate Editor Y. Yuan. (Corresponding author: Chenguang Yang.)

Chengguo Liu and Junyang Li are with the State Key Laboratory of Mechanical Transmission for Advanced Equipment, Chongqing University, Chongqing 400044, China (e-mail: liuchengguo@stu.cqu.edu.cn; junyangli@cqu.edu.cn).

Kai Zhao is with the School of Automation, Chongqing University, Chongqing 400044, China (e-mail: zhaokai@cqu.edu.cn).

Weiyong Si is with the Robotics and Embedded Intelligent Systems Laboratory, University of Essex, CO4 3SQ Colchester, U.K. (e-mail: w.si@essex.ac.uk).

Chenguang Yang is with the Department of Computer Science, University of Liverpool, L69 3BX Liverpool, U.K. (e-mail: cyang@ieee.org).

Color versions of one or more figures in this article are available at https://doi.org/10.1109/TCYB.2025.3555104.

Digital Object Identifier 10.1109/TCYB.2025.3555104

I. Introduction

N RECENT decades, as robotics technology continues to advance, robots have been widely deployed across various fields, including medical rehabilitation [1], industrial manufacturing [2], services [3], and agriculture [4]. Unlike traditional robotic work cells, which often necessitate isolation from human operators for safety reasons, there is a growing demand for effective human–robot interaction (HRI) in modern applications [5], [6]. For instance, in scenarios involving exoskeletons [7], enabling interaction between humans and robots tends to yield better performance compared to fully automated processes. However, in contrast to noninteractive behaviors that are mainly concerned with motion control, HRI expects the robot to respond dynamically to human actions, which poses a challenge for controller design.

Ensuring that robots can accurately perceive human potential intentions is crucial for fulfilling task requirements while minimizing the human effort in HRI. Given the effectiveness of human motor control, a dynamic movement primitive-based observer in [8] is employed to estimate human motion intention (HMI), but this approach relies on offline demonstrations. In [9], a minimum jerk model is used to define the human desired motion, with model parameters identified using the least squares method. However, this method requires prior knowledge of corresponding kinematics, making it difficult to apply to dynamic interaction applications. In [10], a shared control strategy is proposed for recognizing the intention of operators and enabling the robot to provide motion assistance. In [11], a hybrid visual-haptic framework is designed to perform the estimation of human intentions, thus ensuring motion synchronization in human–robot co-transportation. In [12], a neural network (NN)-based online approximation method is proposed to estimate unknown HMI in collaboration tasks. In [13], a Bayesian method is applied for the motion intention inference. In [14], an interactive cooperative control strategy is developed, allowing the exoskeleton robot to perceive variable HMI and track human movements, thereby enhancing collaborative performance. However, estimating HMI alone is insufficient to achieve the ideal HRI, as operators also expect the robot to exhibit human-like compliance characteristics for natural and stable interaction.

Impedance/Admittance control is widely regarded as one of the most reliable methods for HRI [15], [16], [17], [18],

primarily due to its inherent physical basis of second-order systems and the mechanical properties of biomimetic systems. which equips the robot with the ability to flexibly regulate the force-position relationship and adapt to uncertain human motion. However, the traditional impedance/admittance method usually difficult to achieve the desired interaction performance in human-guided tasks [19], [20], [21], [22]. For this reason, the work in [19] develops an adaptive impedance method to reduce the human effort required during the interaction, incorporating online and iterative learning algorithms of impedance parameters for nonrepetitive and repetitive tasks, respectively, to ensure the interaction stability. In [20], an adaptive impedance algorithm inspired by bionic control is proposed to obtain the desired robot compliance. The work in [21] introduces a variable admittance control, where the damping term is adaptively updated based on the sensed interaction force, facilitating smooth human-robotenvironment interaction while maintaining system passivity. In [22], a robust admittance control is designed for human robot cooperation under unknown loads. In addition, the surface electromyography (sEMG) signal has been widely used in HRI [5], [23] due to its advantage of directly reflecting human muscle activity and being generated before the motion actually happens [24]. In [25], an endpoint stiffness identification method for robot impedance skill learning is formed by combining the sEMG and the human upper limb dynamics model, in which the collected raw sEMG signals are smoothed and filtered using a moving average process and a low-pass filter, respectively, to reduce the effect of noise. Other sEMG noise removal methods include empirical mode decomposition [26], signal whitening [27], and independent component analysis [28], but these techniques are computationally expensive [29]. Also, the work in [30] evaluates the assistance efficiency of the fuzzy adaptive admittance control designed for exoskeletons by sEMG signals. However, it is worth noting that these studies primarily focus on the motion planning of the robot during the interaction, often neglecting the actual trajectory accuracy of its low-level controller. Whereas the control result of the admittance model is mainly determined by the performance of the inner-loop position control [16], [17], [30], [31], [32]. Therefore, it is essential to consider the comprehensive tracking capability of the robot in HRI.

Robots are typically modeled as Euler-Lagrangian systems with complex nonlinear properties [33], and NNs, as a popular intelligent tool [34], [35], [36], [37], [38], [39], can be integrated into the controller for effective estimation of unknown dynamics. The work in [37] proposes an NN-based adaptive control for compensating robot uncertainty in HRI to ensure interaction performance. In [38], a neural learning-based trajectory tracking control is proposed for robots considering input saturation, where a radial basis function NN (RBFNN) is used to estimate the lumped uncertainty. To reduce the computational load associated with online updating of the weight matrix, the work in [39] proposes a minimal-learning-parameter technique based on adaptive NN for function approximation. Further, robots are expected to achieve faster response and higher accuracy. Prescribed

performance control (PPC), formed by incorporating the prescribed performance function (PPF) into the control design. has been shown to be very effective in managing output constraints of the system [32], [40], [41], [42], [43]. In detail, the work in [43] addresses the complexity explosion inherent in backstepping techniques by integrating a command filter (CF) and an error compensation mechanism (ECM) into the controller, alongside an error transformation function to achieve performance constraints. In [32], an approximationbased admittance controller that combines force and trajectory adaptation with performance constraints is designed to enable robots to compliantly interact with unknown environments. To further enhance the response speed, the work in [44] introduces an adaptive control method based on predefined time PPF, which enables the teleoperation system to be equipped with trajectory tracking capability with specified transient performance. In [45], an adaptive predefined time control is designed based on the barrier Lyapunov function to realize the full-state error constraint of nonlinear systems. However, classical PPC relies on the initial state of the system, leading to semi-global results. When the desired signal changes, it is necessary to reassess whether the control parameters are valid under the new conditions, thus limiting its application [46], [47]. To fill this gap, the work in [31] presents a switching mechanism to implement the global error constraints for interaction systems constructed by the admittance model. In [48], a shift function is proposed to ensure that the tracking accuracy of the robot under arbitrary initial conditions is within the desired performance range. Nevertheless, it should be emphasized that the transient convergence time, steady state tracking accuracy and global stability guarantee of the controlled system as well as the adaptive admittance control that combines sEMG signals and HMI are not simultaneously involved in the above works. Based on the aforementioned discussion, the main contributions of this article can be summarized as follows.

- Based on the Lyapunov method, a dynamic updating algorithm is designed to estimate HMI, which is then incorporated into the sEMG-based adaptive admittance control for HRI. In contrast to existing interaction strategies [11], [14], [31], [37], [49], this study enables the robot to understand uncertain human motions during interaction, while leveraging human upper limb muscle activity to modulate its stiffness for human-like compliance, thereby improving interaction accuracy and reducing human effort.
- 2) This study proposes a novel error transformation mechanism incorporating a predefined time PPF to achieve the prescribed performance under arbitrary initial conditions. Unlike current output constraint controllers [31], [32], [44], [45], [48], [50], the designed trajectory tracking method not only ensures that the error remains within specified boundaries but also guarantees the transient predefined time convergence and global control capability of the robotic system in HRI, even under model uncertainty.
- A neuroadaptive admittance control strategy that integrates NN, sEMG signals, HMI estimation, and PPC

is developed for the first time. Building on this, we conduct numerous comparative experiments of trajectory tracking and HRI on a real robot to verify the practical applicability of the proposed method. The results confirm that the controller provides high-quality tracking performance and also ensures natural and stable interaction behavior.

The remainder of this article is organized as follows. Section II describes the specific structure of the system dynamics, admittance model, and RBFNN. Section III designs the neuroadaptive admittance controller based on the summary of existing works. In Section IV, we demonstrate the advantages of the proposed scheme through two sets of experiments on the robot trajectory tracking and the HRI. The conclusion and discussion about the convergence of all states in the closed-loop system are illustrated in the last two sections.

II. PROBLEM STATEMENT

A. System Dynamics

The dynamics of n-link manipulators can be formulated as

$$M(q)\ddot{q} + C(q, \dot{q})\dot{q} + G(q) = \tau + J^{T}F_{h}$$
 (1)

where $M \in \mathbb{R}^{n \times n}$, $C \in \mathbb{R}^{n \times n}$, and $G \in \mathbb{R}^{n \times 1}$ denote the inertia matrix, the centripetal–Coriolis force matrix, and gravity matrix. $q, \dot{q}, \ddot{q} \in \mathbb{R}^n$ denote the position, velocity, and acceleration in joint space. $J \in \mathbb{R}^{m \times n}$ denotes the Jacobian matrix, m denotes the dimension of the considered Cartesian space, $F_h \in \mathbb{R}^m$ denotes the interaction force between the robot and the human, and $\tau \in \mathbb{R}^n$ denotes the control input.

In general, M, C, and G contain uncertain terms, expressed as $M = M_0 - \Delta M$, $C = C_0 - \Delta C$, and $G = G_0 - \Delta G$. M_0 , C_0 , and G_0 denote the nominal parts, ΔM , ΔC , and ΔG denote the other unknown parts. Hence, (1) can be reformulated as follow:

$$\mathbf{M}_0\ddot{\mathbf{q}} + \mathbf{C}_0\dot{\mathbf{q}} + \mathbf{G}_0 = \mathbf{\tau} + \mathbf{\tau}_h + \mathbf{\Delta} \tag{2}$$

where $\Delta = \Delta M\ddot{q} + \Delta C\dot{q} + \Delta G$ denotes model uncertainty.

Similarly, the admittance model in the workspace of the robot can be described as follows:

$$\mathbf{M}_{x}(\ddot{\mathbf{x}}_{c} - \ddot{\mathbf{x}}_{d}) + \mathbf{B}_{x}(\dot{\mathbf{x}}_{c} - \dot{\mathbf{x}}_{d}) + \mathbf{K}_{x}(\mathbf{x}_{c} - \mathbf{x}_{d}) = \mathbf{F}_{h}$$
(3)

where M_x , B_x , $K_x \in \mathbb{R}^{m \times m}$ denote the given inertia, damping and stiffness parameters of admittance model, x_d , \dot{x}_d , $\ddot{x}_d \in \mathbb{R}^m$ denote the human desired position, velocity and acceleration, respectively, and x_c , \dot{x}_c , $\ddot{x}_c \in \mathbb{R}^m$ denote the output command position, velocity and acceleration of the robot end-effector, respectively.

The forward kinematics of robots can be described as

$$x = \psi(q). \tag{4}$$

Accordingly, the inverse kinematics problem is solved by a closed-loop inverse kinematics (CLIKs) algorithm [51] to derive the joint angle q_c from x_c , that is

$$\boldsymbol{q}_c = \kappa(\boldsymbol{x}_c) = \int_0^t \left[\boldsymbol{K}_c \boldsymbol{J}^T (\boldsymbol{x}_c - \psi(\boldsymbol{q})) \right] dt$$
 (5)

where $K_c \in \Re^{n \times n}$ denotes a positive-definite matrix.

From (5), it is not hard to find that this method allows the joint angles to be obtained without computing the inverse of the Jacobian matrix, thus circumventing the numerical drift and improving solution accuracy.

Remark 1: According to the work in [17], we can find that the compliance of robots driven by the admittance model is influenced by the internal position controller. If $q=q_c$, the robot can achieve the desired compliance. However, the model uncertainty of robots will affect the trajectory tracking accuracy. Therefore, one of the focuses of this study is to make q track q_c in a fast and accurate manner. In addition, the human-like variable stiffness property is also included in the subsequent control design.

B. Control Input of Human

In the considered interaction scenario, the human exerts a force to guide the robot in performing the desired motion, which can be described by the following stiffness model [31]:

$$K_h(q_d - q) = \tau_h = J^T F_h \tag{6}$$

where $K_h \in \Re^{n \times n}$ denotes the positive-definite arm stiffness matrix, $q_d \in \Re^n$ denotes the HMI, and $\tau_h \in \Re^n$ denotes the interaction torque in joint space.

In practical HRI, robots and humans typically pursue distinct target motions, each being aware only of their respective goals. As outlined in (1), when $\tau_h = 0$, it indicates that the robot is not under human intervention, thus reducing the problem to a conventional tracking control task. Conversely, if $\tau = 0$, it indicates the absence of motor input from the robot, transforming the problem into one of human motor control as discussed in [52]. Furthermore, in cases where $\tau_h \neq 0$ and $\tau \neq 0$, both robot and human dynamics must be considered simultaneously. However, the HMI is often difficult to obtain in advance. Therefore, the accurate estimation of HMI becomes a critical focus of this study.

C. Neural Networks

The RBFNN provides exceptional approximation capabilities and serves as an effective tool for modeling the uncertain dynamics of controlled systems, and the mathematical representation is given as follows:

$$f(X) = W^T S(X) \tag{7}$$

where $W \in \mathbb{R}^d$ denotes the weight matrix, $X \in \mathbb{R}^l$ denotes the input vector. Here, $d, l \in \mathbb{R}^+$ denote the number of hidden layer nodes and input variables, respectively. The basis function $S(X) \in \mathbb{R}^d$ is chosen in the following form:

$$S_j(X) = \exp(-\|X - C_j\|^2 / \sigma_j^2), j = 1, 2, ..., d$$
 (8)

where $C_j \in \mathbb{R}^l$ and $\sigma_j \in \mathbb{R}^+$ denote the center and width of the *j*th Gaussian function, respectively.

In theory, f(X) can approximate any given function with arbitrary precision, as long as d is sufficiently large for $\forall X \in \Omega_X$. Specifically, it can be expressed as follows:

$$f(X) = W^{*T}S(X) + \varepsilon \tag{9}$$

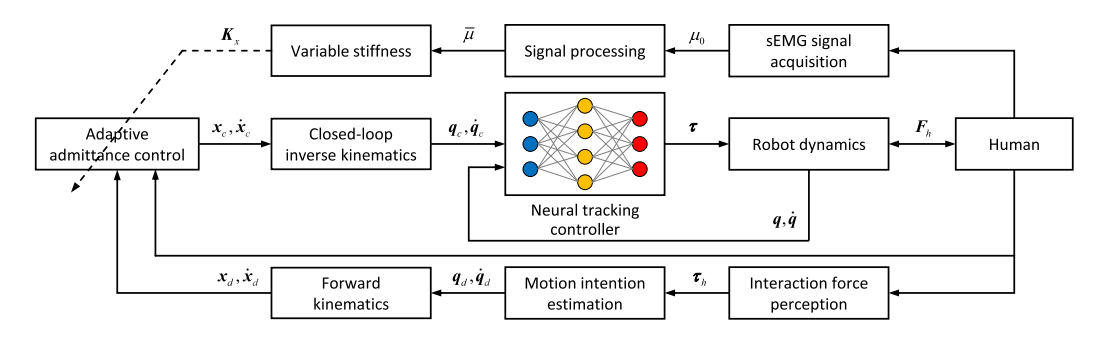


Fig. 1. Block diagram of the designed overall control framework.

where ε denotes the estimation error that is bounded by $|\varepsilon| \le \bar{\varepsilon}$ with $\bar{\varepsilon} > 0$ being a constant. W^* is the optimal weight matrix shown below

$$W^* = \underset{W^* \in \mathbb{R}^d}{\min} \left\{ \sup_{X \in \Omega_X} |f(X) - W^T S(X)| \right\}.$$
 (10)

III. CONTROL DESIGN

Following the previous analysis, this section presents the design of a neuroadaptive admittance control. To begin with, a novel robot neural tracking controller is proposed to realize the output error constraint based on the backstepping technique, NN, and PPC. Next, we develop an adaptive update method for predicting HMI to reduce human effort in HRI. Finally, human upper-limb stiffness is estimated via sEMG signals, which enables the robot can adopt human-like compliance through the admittance control to improve the interaction performance. The overall framework is illustrated in Fig. 1.

A. Output Error Constraint

To ensure the tracking error $e = q - q_c = [e_1, \dots, e_n]^T$ satisfies the desired performance, it needs to be constrained by $-\varrho(t) < e_i(t) < \varrho(t)$ for $t \ge 0$. Here, $\varrho(t)$ denotes the PPF as mentioned in works [41], [48], and is given by the following form:

$$\varrho(t) = (\varrho_0 - \varrho_\infty) \exp(-\phi t) + \varrho_\infty \tag{11}$$

where $\phi > 0$ denotes a parameter affecting error convergence speed, ϱ_0 denotes the initial value, and $0 < \varrho_\infty \ll 1$ denotes the steady-state accuracy range. Therefore, we can find that the classical PPF-based control design must satisfy the prerequisite $-\varrho(0) < e_i(0) < \varrho(0)$, which impacts the global stability and limits its applicability.

To address this gap, this study proposes the following form of PPF:

$$\mathcal{I}(\varrho) = \eta \operatorname{arctanh}(\varrho) \tag{12}$$

where $\eta = \varrho_{\infty}/\arctan(\varrho_{\infty})$, and ϱ is designed in the following form:

$$\varrho(t) = \begin{cases} \left(\frac{\mathcal{T} - t}{\mathcal{T}}\right)^{\phi + 1} (1 - \varrho_{\infty}) + \varrho_{\infty}, \ t \in [0, \mathcal{T}) \\ \varrho_{\infty}, & t \in [\mathcal{T}, \infty) \end{cases}$$
(13)

where \mathcal{T} denotes a predefined convergence time.

Remark 2: It is evident that $\mathcal{I}(\varrho)$ is monotonically decreasing with respect to time, satisfying the necessary conditions for the performance function. Additionally, We can find that $\mathcal{I}(\varrho(0)) = \eta \operatorname{arctanh}(1) \to +\infty$, indicating that it can accommodate any initial system condition and achieve global results during HRI. Meanwhile, $\mathcal{I}(\lim_{t\to\infty}\varrho(t)) = \mathcal{I}(\varrho(\mathcal{T})) = \eta \operatorname{arctanh}(\varrho_\infty) = \varrho_\infty$ can be adjusted to meet specific task requirements, ensuring tracking accuracy. Furthermore, the error convergence time \mathcal{T} is also user-defined, allowing for improved transient performance.

B. Error Transformation Mechanism

Next, we design the following normalized function:

$$\chi(e_i) = \tanh\left(\frac{e_i}{\eta}\right). \tag{14}$$

It is not difficult to find that $\chi(e_i)$ has the following characteristics: 1) $\chi(e_i)$ is strictly monotonic with respect to $e_i \in \Re$; 2) $\chi(e_i) \in (-1, 1)$ always holds; and 3) when $e_i \to \infty$, $\chi(e_i) \to 1$, when $e \to -\infty$, $\chi(e) \to -1$, and only when $e_i = 0$, $\chi(e_i) = 0$. Additionally, it holds that $e_i = \mathcal{I}(\chi)$.

Further, the following error transformation is proposed:

$$\theta_i = \frac{\lambda}{(1+\lambda)(1-\lambda)} \tag{15}$$

where θ_i denotes the transformed error and $\lambda(t) = \chi(e_i)/\varrho(t)$. In accordance with the definition of $\chi(e_i)$ and $\varrho(t)$, we can know that $\lambda(0) = \chi(e_i(0))/\varrho(0)$. Then, it is worth noting that only when $\lambda \to \pm 1$, $\theta_i \to \infty$. In summary, for $\forall t > 0$, if the designed tracking controller is capable of ensuring that θ_i remains bounded, the result $-1 < \lambda(t) < 1$ will always hold. Thus

$$-\varrho(t) < \chi(e_i) < \varrho(t) \tag{16}$$

$$\mathcal{I}(-\rho) < \mathcal{I}(\chi) < \mathcal{I}(\rho).$$
 (17)

Considering the fundamental characteristics of odd function $\mathcal{I}(\varrho)$ and the fact of $e_i(t) = \mathcal{I}(\chi)$, the below inequality can be established

$$-\mathcal{I}(\varrho) < e_i(t) < \mathcal{I}(\varrho). \tag{18}$$

Here, it is easy to find that we reduce the problem of constraining the original trajectory tracking error $e_i(t)$ within the PPF $\mathcal{I}(\varrho)$ to the more manageable problem of ensuring that the transformed error θ_i is bounded for all t > 0, and the

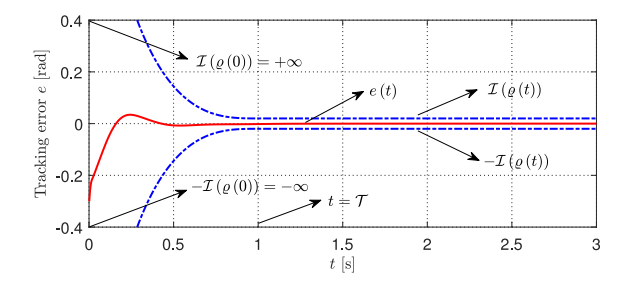


Fig. 2. Graphical representation of the output constraint controller with $\mathcal{T}=1$.

corresponding graphical representation of the output constraint controller is shown in Fig. 2.

Further, we can know that $\dot{\theta}_i$ is required in the design of the adaptive control using the backstepping technique. Accordingly, it can be obtained by differentiating (15)

$$\dot{\theta_i} = \frac{(1+\lambda^2)\dot{\lambda}}{(1-\lambda^2)^2} \tag{19}$$

with

$$\dot{\lambda} = \frac{(\dot{\chi}\varrho - \chi\dot{\varrho})}{\rho^2}, \quad \dot{\chi} = \frac{\dot{e}_i}{\eta} \left[1 - \tanh^2 \left(\frac{e_i}{\eta} \right) \right]. \tag{20}$$

Therefore, the specific mapping of $\dot{\theta}_i$ to \dot{e}_i can be derived by substituting (20) into (19)

$$\dot{\theta}_{i} = \varpi_{1i}\dot{e}_{i} + \varpi_{2i}$$

$$= \frac{\left(1 + \lambda^{2}\right)\left[1 - \tanh^{2}\left(\frac{e_{i}}{\eta}\right)\right]\dot{e}_{i}}{\left(1 - \lambda^{2}\right)^{2}\eta\varrho} - \frac{\left(1 + \lambda^{2}\right)\chi\dot{\varrho}}{\left(1 - \lambda^{2}\right)^{2}\varrho^{2}} \tag{21}$$

where

$$\varpi_{1i} = \frac{\left(1 + \lambda^2\right) \left[1 - \tanh^2\left(\frac{e_i}{\eta}\right)\right]}{\left(1 - \lambda^2\right)^2 \eta \varrho} \tag{22}$$

$$\varpi_{2i} = -\frac{\left(1 + \lambda^2\right)\chi\dot{\varrho}}{\left(1 - \lambda^2\right)^2\varrho^2}.$$
 (23)

C. Neural Tracking Control

Based on (2) and (15), we define the following error system:

$$\begin{cases} z_1(t) = \boldsymbol{\theta}(t) \\ z_2(t) = \dot{\boldsymbol{q}}(t) - \bar{\boldsymbol{\alpha}}(t) \end{cases}$$
 (24)

$$\begin{cases} v_1(t) = z_1(t) - \xi_1 \\ v_2(t) = z_2(t) - \xi_2 \end{cases}$$
 (25)

where $\bar{\alpha}$ denotes the output of the following CF when the input signal is the virtual control law α

$$\begin{cases} \dot{\varphi}_1 = -\mathbf{r}_1 | \varphi_1 - \alpha |^{\frac{1}{2}} \operatorname{sign}(\varphi_1 - \alpha) + \varphi_2 \\ \dot{\varphi}_2 = -\mathbf{r}_2 \operatorname{sign}(\varphi_2 - \dot{\varphi}_1) \end{cases}$$
 (26)

where $\mathbf{r}_1 = \text{diag}[r_{11}, \dots, r_{1n}]$ and $\mathbf{r}_2 = \text{diag}[r_{21}, \dots, r_{2n}]$ denote control parameters, $\boldsymbol{\varphi}_1$ and $\boldsymbol{\varphi}_2$ denote states.

Remark 3: If the input signal remains unaffected by noise, i.e., $\alpha = \alpha_0$, then $\varphi_1 = \alpha_0$ and $\dot{\varphi}_1 = \dot{\alpha}_0$ hold under appropriate parameter choices with $r_{1i} > 0$ and $r_{2i} > 0$. However, if the signal noise is bounded by a constant v_i , such

that $|\alpha_i - \alpha_{0i}| \le \nu_i$, then the inequalities $|\varphi_{1i} - \alpha_{0i}| \le A_1 \nu_i = o_{1i}$ and $|\dot{\varphi}_{1i} - \dot{\alpha}_{0i}| \le A_2 \nu_i^{1/2} = o_{2i}$ hold, where A_1 and A_2 denote positive constants [53].

Similarly, ξ_1 and ξ_2 represent the error compensation signals which are defined by the following ECM:

$$\begin{cases} \dot{\boldsymbol{\xi}}_1 = -\boldsymbol{k}_1 \boldsymbol{\xi}_1 + \boldsymbol{\varpi}_1 (\boldsymbol{\xi}_2 + (\bar{\boldsymbol{\alpha}} - \boldsymbol{\alpha})) - \boldsymbol{h}_1 \operatorname{sign}(\boldsymbol{\xi}_1) \\ \dot{\boldsymbol{\xi}}_2 = -\boldsymbol{k}_2 \boldsymbol{\xi}_2 - \boldsymbol{h}_2 \operatorname{sign}(\boldsymbol{\xi}_2) \end{cases}$$
(27)

where $\boldsymbol{\varpi}_1 = \operatorname{diag}[\boldsymbol{\varpi}_{1i}, \dots, \boldsymbol{\varpi}_{1n}], \ \boldsymbol{k}_1 = \operatorname{diag}[k_{11}, \dots, k_{1n}], \ \boldsymbol{h}_1 = \operatorname{diag}[h_{11}, \dots, h_{1n}], \ \boldsymbol{k}_2 = \operatorname{diag}[k_{21}, \dots, k_{2n}], \ \operatorname{and} \ \boldsymbol{h}_2 = \operatorname{diag}[h_{21}, \dots, h_{2n}] \ \operatorname{denote} \ \operatorname{designed} \ \operatorname{control} \ \operatorname{parameters}.$

Remark 4: Since the controller design requires the term $\dot{\alpha}$, direct differentiation of α would amplify noise, hence increasing the tracking error and affecting the system stability. To address this issue, we introduce a CF (26) to maintain signal continuity and accuracy. However, the employment of CF inevitably generates filter errors. Consequently, the main purpose of developing an ECM (27) is to compensate for these errors and enhance control performance.

Then, we introduce the following Lyapunov function:

$$V_1 = \frac{1}{2} \mathbf{v}_1^T \mathbf{v}_1. \tag{28}$$

Derivation of V_1 yields

$$\dot{V}_1 = \mathbf{v}_1^T \dot{\mathbf{v}}_1 = \mathbf{v}_1^T (\boldsymbol{\varpi}_1 \dot{\boldsymbol{e}} + \boldsymbol{\varpi}_2 - \dot{\boldsymbol{\xi}}_1)
= \mathbf{v}_1^T (\boldsymbol{\varpi}_1 (\mathbf{v}_2 + \boldsymbol{\xi}_2 + \bar{\boldsymbol{\alpha}} - \dot{\boldsymbol{q}}_c) + \boldsymbol{\varpi}_2 - \dot{\boldsymbol{\xi}}_1).$$
(29)

Thus, we design the virtual control law α as follow:

$$\boldsymbol{\alpha} = \dot{\boldsymbol{q}}_c - \boldsymbol{\omega}_1^{-1} (\boldsymbol{k}_1 \boldsymbol{z}_1 + \boldsymbol{\omega}_2) \tag{30}$$

where $\boldsymbol{\varpi}_2 = [\varpi_{2i}, \dots, \varpi_{2n}]^T$.

Substituting (30) into (29), one can get

$$\dot{V}_1 = -v_1^T k_1 v_1 + v_1^T \boldsymbol{\varpi}_1 v_2 + \boldsymbol{h}_1 v_1 \operatorname{sign}(\boldsymbol{\xi}_1).$$
 (31)

Next, consider the 2-nd Lyapunov function

$$V_2 = V_1 + \frac{1}{2} v_2^T v_2. (32)$$

Taking the derivative of V_2 yields

$$\dot{V}_{2} = -\mathbf{v}_{1}^{T} \mathbf{k}_{1} \mathbf{v}_{1} + \mathbf{v}_{2}^{T} \dot{\mathbf{v}}_{2}
+ \mathbf{v}_{1}^{T} \boldsymbol{\varpi}_{1} \mathbf{v}_{2} + \mathbf{h}_{1} \mathbf{v}_{1} \operatorname{sign}(\boldsymbol{\xi}_{1})
= -\mathbf{v}_{1}^{T} \mathbf{k}_{1} \mathbf{v}_{1} + \mathbf{v}_{2}^{T} (\boldsymbol{\varpi}_{1} \mathbf{v}_{1} + \boldsymbol{F} - \dot{\boldsymbol{\alpha}} + \mathbf{k}_{2} \boldsymbol{\xi}_{2})
+ \mathbf{v}_{2}^{T} (\boldsymbol{M}_{0}^{-1} (\boldsymbol{\tau} - \boldsymbol{\tau}_{h} - \boldsymbol{C}_{0} \dot{\boldsymbol{q}} + \boldsymbol{G}_{0}))
+ \mathbf{v}_{1}^{T} \boldsymbol{h}_{1} \operatorname{sign}(\boldsymbol{\xi}_{1}) + \mathbf{v}_{2}^{T} \boldsymbol{h}_{2} \operatorname{sign}(\boldsymbol{\xi}_{2})$$
(33)

where $F(X) = M_0^{-1}\Delta = [f_1(X), \dots, f_n(X)]^T$ denotes the unknown nonlinear term that will be approximated by RBFNN, i.e., $f_i(X) = W_i^{*T}S_i(X) + \varepsilon_i$ with the input variable is defined as $X = [q^T, \dot{q}^T, \bar{\alpha}^T, \dot{\bar{\alpha}}^T]^T$.

Finally, we formulate the 3-rd Lyapunov function as

$$V_3 = V_2 + \frac{1}{2} (\boldsymbol{q}_d - \boldsymbol{q})^T \boldsymbol{K}_h (\boldsymbol{q}_d - \boldsymbol{q}). \tag{34}$$

Derivation of (34) gives

$$\dot{V}_3 = \dot{V}_2 + (\dot{\boldsymbol{q}}_d - \dot{\boldsymbol{q}})^T \boldsymbol{\tau}_h. \tag{35}$$

Based on (33) and (35), we develop τ as

$$\boldsymbol{\tau} = \boldsymbol{C}_0 \dot{\boldsymbol{q}} + \boldsymbol{G}_0 + \boldsymbol{\tau}_h + \boldsymbol{M}_0 \left(-\boldsymbol{\varpi}_1 \boldsymbol{v}_1 - \hat{\boldsymbol{W}}^T \boldsymbol{S}(\boldsymbol{X}) - \boldsymbol{k}_2 \boldsymbol{z}_2 + \dot{\boldsymbol{\alpha}} \right) + \boldsymbol{M}_0 \left(\boldsymbol{v}_2^T \right)^+ \left[\left(\dot{\boldsymbol{q}} - \dot{\boldsymbol{q}}_d \right)^T + \left(\boldsymbol{q}_d - \boldsymbol{q} \right)^T - \dot{\boldsymbol{q}}_d^T \right] \boldsymbol{\tau}_h$$
 (36)

where $(v_2^T)^+$ denotes the Moore-Penrose inverse of v_2^T , \hat{W} denotes the estimated of W^* , and $\tilde{W} = W^* - \hat{W}$ denotes the estimation error matrix.

The adaptive law of \hat{W}_i is designed as

$$\dot{\hat{\boldsymbol{W}}}_{i} = \boldsymbol{Q}_{i} \left[v_{2i} \boldsymbol{S}_{i}(\boldsymbol{X}) - p \hat{\boldsymbol{W}}_{i} \right], i = 1, \dots, n$$
 (37)

where Q_i denotes a positive definite symmetric matrix and p denotes a positive constant.

To model the HMI in the interaction process, we propose the following adaptive update law for q_d :

$$\dot{q}_d = \rho \tau_h \tag{38}$$

where ρ denotes a positive definite symmetric matrix. Substituting (36) and (38) into (35), one can get

$$\dot{V}_{3} = -\mathbf{v}_{1}^{T} \mathbf{k}_{1} \mathbf{v}_{1} - \mathbf{v}_{2}^{T} \mathbf{k}_{2} \mathbf{v}_{2} - \mathbf{\tau}_{h}^{T} \boldsymbol{\rho} \mathbf{\tau}_{h}$$

$$- (\mathbf{q}_{d} - \mathbf{q})^{T} \mathbf{K}_{h} (\mathbf{q}_{d} - \mathbf{q}) + \sum_{i=1}^{n} \mathbf{v}_{2i} \tilde{\mathbf{W}}_{i}^{T} \mathbf{S}_{i}$$

$$+ \mathbf{v}_{1}^{T} \mathbf{h}_{1} \operatorname{sign}(\boldsymbol{\xi}_{1}) + \mathbf{v}_{2}^{T} \mathbf{h}_{2} \operatorname{sign}(\boldsymbol{\xi}_{2}) + \mathbf{v}_{2}^{T} \boldsymbol{\varepsilon}. \quad (39)$$

The below theorem consolidates the stability guarantee and interaction performance of the proposed controller.

Theorem 1: For the robotic system (1) that interacts with humans exhibiting unknown motion behavior, the combined application of the virtual controller (30), the adaptive update laws (37) and (38), and the control input (36) not only accurately estimates the HMI q_d but also effectively ensures the trajectory error e converges to the given performance constraint boundary range within a predefined time \mathcal{T} . Furthermore, the global stability of the system can be achieved.

Proof: See the Appendix.

D. Adaptive Admittance Control

Driven by the designed neural tracking controller, it is assumed that $q \approx q_c$, and thus the robot can attain approximately ideal compliance performance. Further, the human-like variable stiffness characteristic is derived based on the sEMG signal, which is associated with human muscle activity and can be obtained from the MYO armband. First, we preprocess the raw sEMG signals of all channels in the following way:

$$\mu_0(t) = \frac{1}{N} \sum_{i=1}^{N} |\text{sEMG}_i(t)|$$
 (40)

where N=8 denotes channels number of MYO, sEMG_i(t) denotes the raw signal, and $\mu_0(t)$ denotes the processed signal. Then, we employ the moving average technique [25] for $\mu(t)$

$$\mu(t) = \frac{1}{D} \sum_{k=0}^{D-1} \mu_0(t-k)$$
 (41)

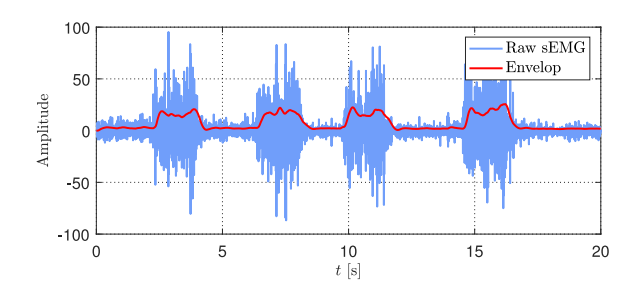


Fig. 3. Envelope obtained from the raw sEMG signal.

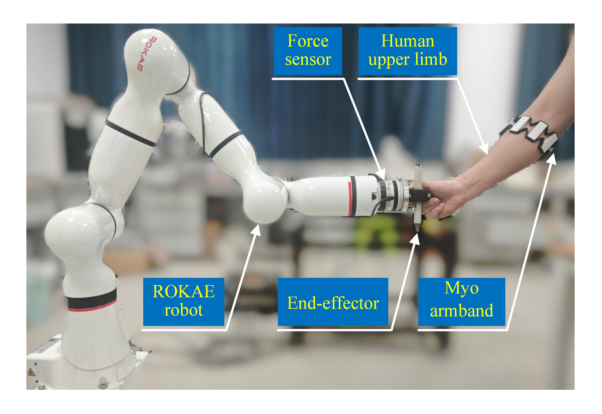


Fig. 4. Experimental setup.

where D denotes the window length. Also, a low-pass filter with the cut-off frequency of 2.5 (Hz) is used to treat $\mu(t)$ to obtain the envelope $\mu_f(t)$, which is shown in Fig. 3.

Thus, we establish the following mapping relationship [24]:

$$\wp = \frac{1 - e^{-\varphi\bar{\mu}}}{1 + e^{-\varphi\bar{\mu}}} \quad \text{with} \quad 0 \le \bar{\mu} = \frac{\mu_f}{\mu_{\text{max}}} \le 1 \quad (42)$$

where \wp denotes the index, and φ denotes a positive constant. Therefore, the mapping relationship among \wp and K is provided by the following:

$$K_{x} = \wp(K_{\text{max}} - K_{\text{min}}) + K_{\text{min}} \tag{43}$$

where K_{max} and K_{min} denote the maximum and minimum values of the stiffness variation, which can be set through prior experimentation. Hence, with the proposed adaptive admittance control, the robot can dynamically mimic human stiffness to ensure high-quality interactions.

In summary, precise trajectory tracking and regulation of the robot are achieved through HMI prediction, global PPC, and adaptive admittance control, while simultaneously reducing the human effort required in performing HRI. The main steps of the proposed neuroadaptive admittance control can be concluded in Algorithm 1.

IV. EXPERIMENTS

In this section, we will demonstrate the effectiveness of the proposed framework through two sets of experiments, including trajectory tracking and HRI tasks. The experimental study is implemented on the ROKAE robot presented in Fig. 4.

Algorithm 1: Neuroadaptive Admittance Control Based on HMI Estimation and Output Error Constraint

```
Input:
```

The constant matrices/coefficients: k_1 , k_2 , \mathcal{T} , ϕ , ϱ_{∞} , r_1 , r_2 , h_1 , h_2 , Q, p, μ , M_x , B_x , K_{\min} , K_{\max} , φ , D. Output:

The joint drive torque: τ .

1 begin

5

6

7

8

9

10

11

12

- Move the robot to the set initial position;
- Initialize the parameters q_d , \dot{q}_d and τ ;
- 4 | **for** each time step t **do**

Get the interaction force F_h and sEMG signal μ , calculate HMI q_d , \dot{q}_d and stiffness matrix K_x using (38) and (43), respectively.

Compute joint command motion trajectory q_c , \dot{q}_c by admittance model (3) and CLIK (5).

Sense the robot current states q, \dot{q} and compute the error system v_1 , v_2 by (24) and (25).

Derive the virtual controller α using (30).

Update the adaptive NN weight \hat{W} by (37).

Calculate the joint drive torque τ using (36).

Send the generated control input to the robotic actuators using (1).

end for

13 end

A. Results of the Trajectory Tracking Controller

This experiment evaluates the performance of the designed trajectory tracking controller, and joints 1–4 are driven to execute the given motion for simplifying the analysis and remain general. Then, we define the initial state of the robot as $\mathbf{q}_0 = [0, 0.3, 0, 1.57]^T$, and the desired trajectory is set as

$$\mathbf{q}_{d} = \begin{bmatrix} 0.1\sin(t) + 0.3\cos(t) \\ 0.3 + 0.1\sin(t) \\ 0.1\sin(t) - 0.3\cos(t) \\ 1.57 + 0.3\cos(t) \end{bmatrix}$$
(rad). (44)

To validate the advantages of the proposed method, we compare three different methods, i.e., M1: the PD control with the form $\tau = -k_p e - k_d \dot{e} + G_0$; M2: the output constraint control proposed in [48]; and M3: the neural tracking control proposed in this article. The parameters of M1 are given as $k_p = \text{diag}[135, 135, 135, 135]$ and $k_d =$ diag[62, 62, 62, 62]. Similarly, the parameters of M3 are set to $k_1 = \text{diag}[10, 20, 15, 10], k_2 = \text{diag}[30, 45, 35, 30],$ $r_1 = \text{diag}[12, 12, 15, 12], r_2 = \text{diag}[12, 12, 15, 12], h_1 =$ $diag[0.01, 0.01, 0.01, 0.01], h_2 = diag[0.01, 0.01, 0.01, 0.01],$ $Q = \text{diag}[1, 1, 1, 1], \ \phi = 3, \ T = 3, \ \varrho_{\infty} = 0.02, \ \text{and} \ p = 1.$ For RBFNN, the centers of the network are evenly spaced in the interval $[-3, 3] \times [-3, 3] \times [-3, 3] \times [-3, 3] \times [-3, 3] \times$ $[-3, 3] \times [-3, 3] \times$ $[-3, 3] \times [-3, 3] \times [-3, 3] \times [-3, 3] \times [-3, 3]$ and the width is set to 10. Notably, the control gains of M2 are the same as those of M3 for fairness consideration.

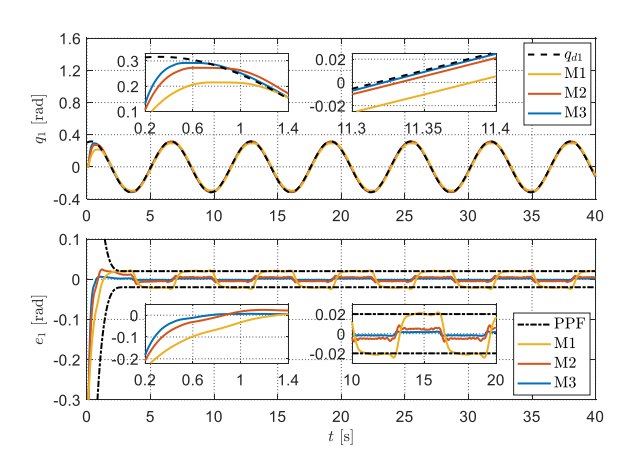


Fig. 5. Tracking trajectory and error of the joint 1.

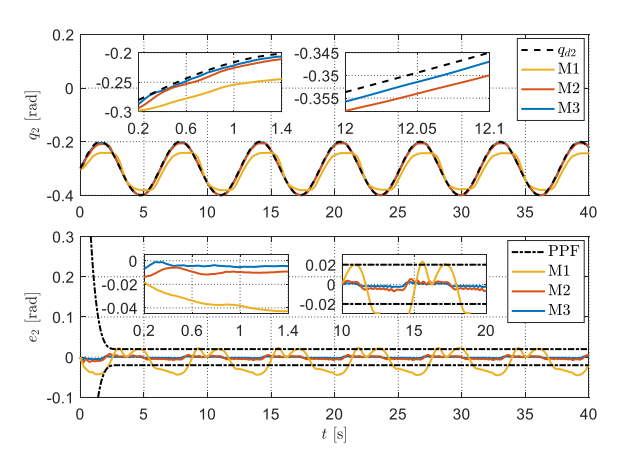


Fig. 6. Tracking trajectory and error of the joint 2.

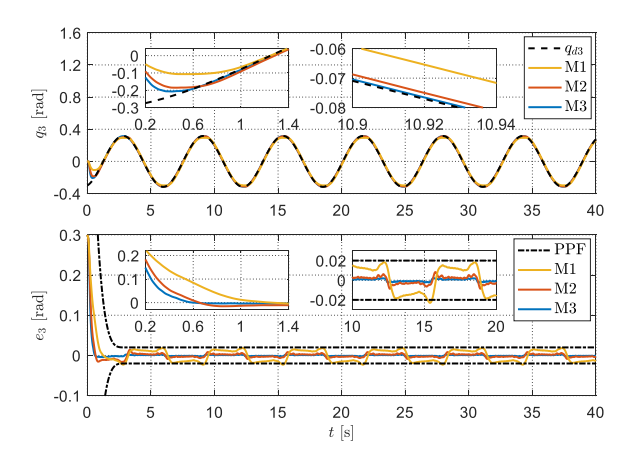


Fig. 7. Tracking trajectory and error of the joint 3.

Figs. 5–8 show the tracking performance and trajectory error for joints 1–4. It is easy to notice that M1 possesses the slowest convergence speed with the lowest tracking accuracy, and its maximum error is beyond the specific performance range. Similarly, although the errors of both M2 and M3 are constrained by the desired performance metrics, M3 consistently outperforms M2 in both transient and steady-state performance, regardless of whether there is a jump in the initial conditions. Moreover, the proposed output constraint control

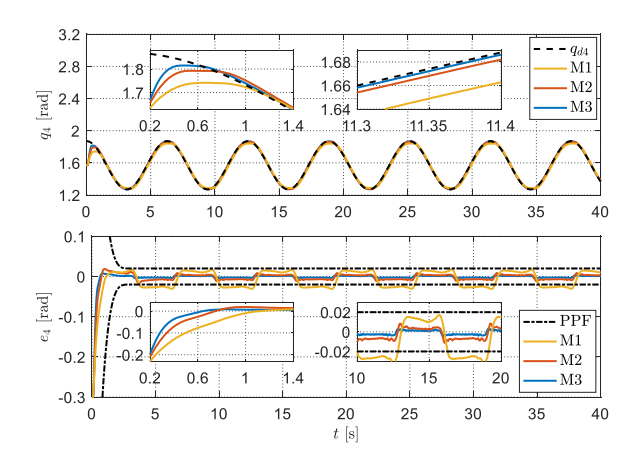


Fig. 8. Tracking trajectory and error of the joint 4.

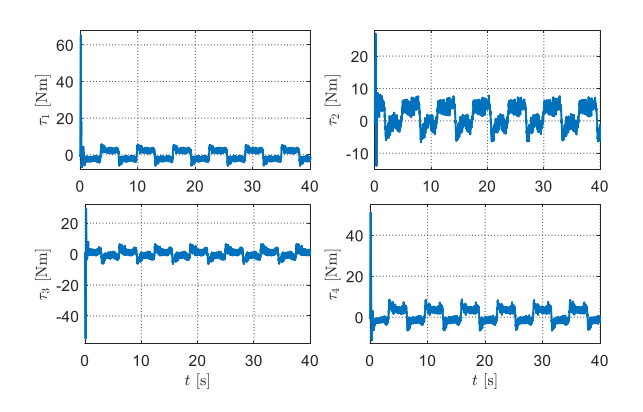


Fig. 9. Control input torque of the proposed method.

method effectively addresses the dependency of traditional PPC methods on the initial state of systems, thereby satisfying the global stability guarantee. Fig. 9 illustrates the control input torque of M3. Given that the torque limits for the tested joints are all 85 (Nm), the actual drive commands remain within this allowable threshold, further validating the practicality of the proposed approach. Additionally, we employ the Root Mean Square Error with RMSE = $\sqrt{(1/m)\sum_{i=1}^{m} e_i^2}$ to quantitatively evaluate and compare the steady-state errors of these methods. The specific results are presented in Fig. 10, where it is evident that the proposed method offers superior control capability across all joints. In conclusion, this approach not only effectively reduces the impact of robot dynamic model uncertainty, but also ensures both transient global predefined time convergence and steady-state high-precision trajectory tracking of the system.

B. Results of the Human-Robot Interaction Controller

This experiment assesses the performance of the designed interaction controller, and we performed a comparison of three different control strategies, i.e., C1: the traditional admittance model with zero stiffness; C2: the force-based variable admittance control proposed in [21]; and C3: the neuroadaptive admittance control proposed in this article. The specific experimental procedure is that the human guides the robot to follow a desired trajectory

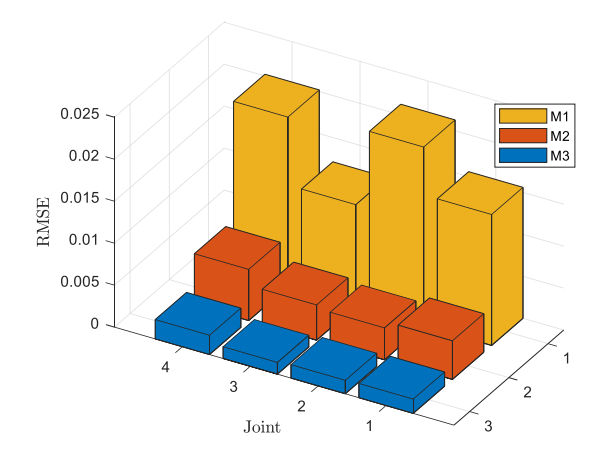


Fig. 10. RMSE analysis of the steady-state performance for different methods.



Fig. 11. Experimental scenario of HRI.

[4.45+8 sin([$2\pi t/T$]), 62.86+16 sin([$2\pi t/T$]) cos([$2\pi t/T$])]^T (cm) as shown in Fig. 11, and it is worth noting that the robot is not aware of this trajectory beforehand. The core objective of the experiment is to equip the robot with human-like stiffness and the ability to understand HMI, thereby facilitating natural HRI. In other words, we aim to ensure precise position tracking while reducing the human effort required during the interaction process. The control parameters of C3 are set as: $\rho = \text{diag}[0.02, 0.02], M_x = \text{diag}[1, 1]$ (kg), $M_x = \text{diag}[200, 200]$ (N/m), $M_x = \text{diag}[200, 200]$ (N/m), M

Fig. 12 shows the experimental tracking trajectories achieved under different controllers and Figs. 13 and 14 illustrate the position errors and interaction forces along the X- and Y- axes. We observe that when dealing with the complex curved trajectory, the constant large damping term in C1, combined with the absence of HMI, leads to sluggish interactions, placing greater demands on the human to guide the robot, which in turn increases tracking error and interaction force. In contrast, C2 adaptively adjusts the damping based on sensed force information, thereby reducing interaction forces and improving tracking accuracy. However, the damping term in this control structure is highly sensitive to interaction

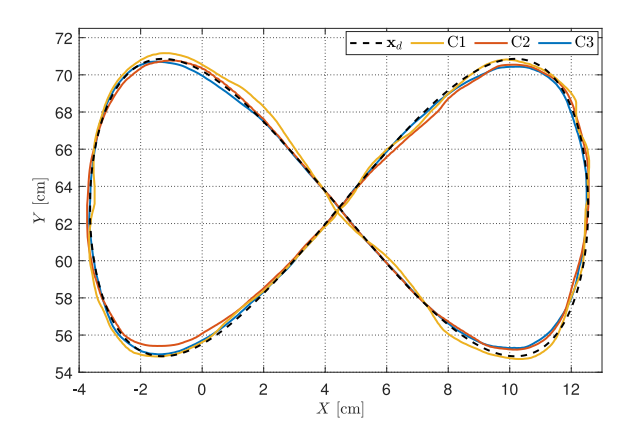


Fig. 12. Motion trajectories of the robot.

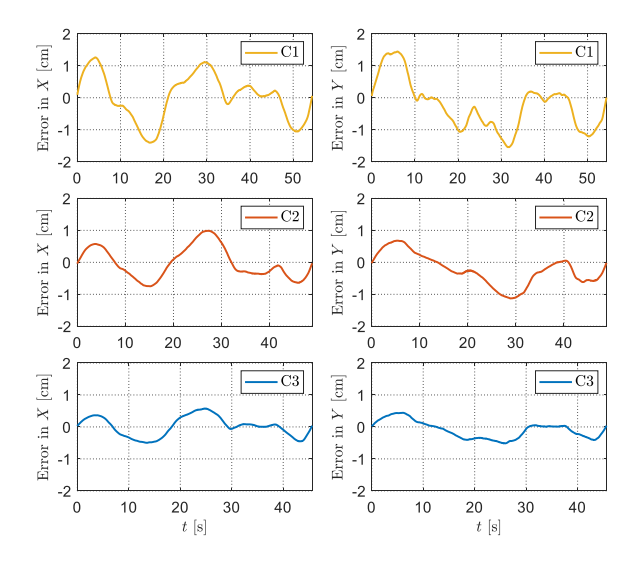


Fig. 13. Position errors of the robot.

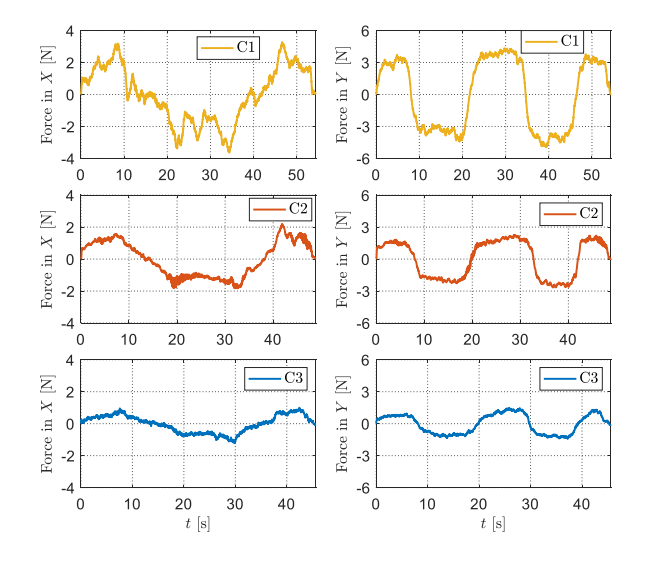


Fig. 14. Interaction forces of the robot.

forces, meaning that the inevitable physiological tremors of the human arm would significantly affect the stability of the robotic system. Based on the above considerations, C3 dynamically predicts HMI while managing the compliance level of the robot by the muscle activity of the human operator,

TABLE I QUANTITATIVE COMPARISON OF POSITION ERROR

Control strategy	Track direction	Position error analysis [cm] MaxE ME AE SD				
	X-axis	1.4072	0.0307	0.5932	0.7207	
	Y-axis X-axis	1.5465 0.9875	-0.2395 -0.0151	0.6393 0.4291	0.7693 0.4944	
C2	Y-axis	1.1294 0.5742	-0.2301 0.0138	0.4403 0.2563	0.4865 0.3112	
C3	X-axis Y -axis	$0.5742 \\ 0.5141$	-0.0138 -0.0939	0.2563 0.2362	$0.3112 \\ 0.2701$	

TABLE II QUANTITATIVE COMPARISON OF INTERACTION FORCE

Control	Track	Interaction force analysis [N]				
strategy	direction	MaxE	ME	AE	SD	
C1	X-axis	3.9429	0.0032	1.5747	1.8782	
CI	Y-axis	4.9496	0.0035	3.1206	3.2784	
C2	X-axis	2.1872	-0.0056	0.9947	1.0997	
C2	Y-axis	2.6619	0.0048	1.6381	1.7299	
C3	X-axis	1.3915	-0.0036	0.5348	0.6245	
63	Y-axis	1.6929	-0.0038	0.9619	1.0401	

TABLE III
AVERAGE NORM OF POSITION ERROR

	S1	S2	S3	S4	S5	S6
C1	0.9342	1.0651	0.9872	1.1739	0.8382	0.7942
C2	0.6526	0.7191	0.6198	0.6956	0.7664	0.5375
C3	0.3158	0.2923	0.4132	0.2761	0.3705	0.3696

effectively enhancing the control capability of the interaction system. Consequently, C3 obtains the smallest position error and interaction force, as well as the system stability is also guaranteed, thus allowing the human to perform interaction tasks more easily, efficiently, and reliably. Further, we employ the following quantitative analysis metrics to verify the comprehensive performance of these comparison controllers, i.e., Maximum Error: MaxE = max{ $|e_i|$ }, Mean Error: ME = $(1/n) \sum_{i=1}^n e_i$, Absolute Error: AE = $[1/n] \sum_{i=1}^n |e_i|$, and Standard Deviation: SD = $\sqrt{(1/n-1) \sum_{i=1}^n |e_i| - \text{ME}|^2}$.

Tables I and II provide the quantitative analysis covering the above metrics for the position tracking error and interaction force of the robot in various controllers. The results demonstrate that the designed method exhibits excellent control performance in all aspects.

Also, we recruit six healthy subjects (three males and three females), aged from 25 to 40, to perform the above interaction task five times under each of the three controllers. All participants provide informed consent prior to the study. Notably, the operators have no idea which control mode the robot is configured in each interaction experiment. Furthermore, we define the following human effort J used to measure interaction sensitivity:

$$J = \int_0^T \left| \mathbf{F}_h(t)^T \mathbf{v}_s(t) \right| dt \tag{45}$$

where T denotes the task duration and $v_s(t)$ denotes the synergy velocity of the system.

Tables III and IV show the average norm of the position error and the interaction force for the human operators

TABLE IV AVERAGE NORM OF INTERACTION FORCE

	S 1	S2	S3	S4	S5	S6
C1	3.7104	4.6723	3.4862	3.9103	4.3173	3.5853
C2	2.0107	1.9196	2.3382	2.1031	2.6856	2.2561
C3	1.2405	1.1679	1.2848	1.0212	1.4386	1.5296

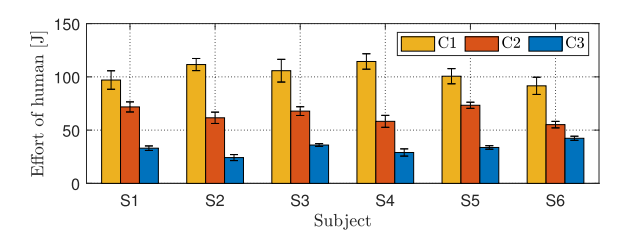


Fig. 15. Statistical results for average effort of human.

throughout the interaction task, respectively. We can find that the error and force are slightly reduced with the force-based variable admittance control [21] compared to the traditional admittance control, and even more so by using the proposed neuroadaptive admittance control. Fig. 15 shows the statistical results for the average effort of humans, and it can be clearly seen that the proposed method outperforms the others and takes the least amount of effort. Therefore, these results indicate that the designed strategy greatly improves the manoeuvrability and control performance of the interaction system.

V. CONCLUSION

This article introduces a novel active control method for HRI that enables the robot to adaptively regulate its trajectory to ensure natural interaction. The HMI is estimated by the sensed force information and the stiffness matrix is adjusted using sEMG signals from the human upper limb, both of which are then fed into the admittance model-controlled robot for human-like interaction characteristics. Further, a PPC based on the error transformation function is designed to realize the global predefined time performance constraint on the output error of the robotic system. With the proposed framework, the robot can quickly and accurately track human expected motion trajectory, as well as reduce human effort while ensuring interaction stability. The experimental results demonstrate the comprehensive control capability of the designed scheme.

However, this study also suffers from the following drawbacks: the estimation accuracy of the HMI is related to the precision of the force sensor, which raises the cost of the application. Furthermore, the model dependence may affect the generality of the controller. Therefore, the design of external force observers and model-free adaptive methods will be considered in future work.

VI. APPENDIX

In this section, the Lyapunov method will be adopted for stability analysis of the HRI system. First, construct the following Lyapunov function candidate:

$$V = V_3 + \frac{1}{2} \sum_{i=1}^{n} \tilde{\boldsymbol{W}}_i^T \boldsymbol{Q}_i^{-1} \tilde{\boldsymbol{W}}_i + \frac{1}{2} \boldsymbol{\xi}_1^T \boldsymbol{\xi}_1 + \frac{1}{2} \boldsymbol{\xi}_2^T \boldsymbol{\xi}_2.$$
 (46)

Take the derivative of V

$$\dot{V} = \dot{V}_{3} + \sum_{i=1}^{n} \tilde{W}_{i}^{T} Q_{i}^{-1} \dot{\tilde{W}}_{i} + \boldsymbol{\xi}_{1}^{T} \dot{\boldsymbol{\xi}}_{1} + \boldsymbol{\xi}_{2}^{T} \dot{\boldsymbol{\xi}}_{2}$$

$$= -\boldsymbol{v}_{1}^{T} \boldsymbol{k}_{1} \boldsymbol{v}_{1} - \boldsymbol{v}_{2}^{T} \boldsymbol{k}_{2} \boldsymbol{v}_{2} - \boldsymbol{\tau}_{h}^{T} \boldsymbol{\rho} \boldsymbol{\tau}_{h}$$

$$- (\boldsymbol{q}_{d} - \boldsymbol{q})^{T} \boldsymbol{K}_{h} (\boldsymbol{q}_{d} - \boldsymbol{q}) - \boldsymbol{\xi}_{1}^{T} \boldsymbol{k}_{1} \boldsymbol{\xi}_{1} - \boldsymbol{\xi}_{2}^{T} \boldsymbol{k}_{2} \boldsymbol{\xi}_{2}$$

$$+ p \sum_{i=1}^{n} \tilde{W}_{i}^{T} \hat{W}_{i} + \boldsymbol{v}_{2}^{T} \boldsymbol{\varepsilon} + \boldsymbol{\xi}_{1}^{T} \boldsymbol{\varpi}_{1} \boldsymbol{\xi}_{2} + \boldsymbol{\xi}_{1}^{T} \boldsymbol{\varpi}_{1} \boldsymbol{o}_{1}$$

$$+ \boldsymbol{v}_{1}^{T} \boldsymbol{h}_{1} \operatorname{sign}(\boldsymbol{\xi}_{1}) + \boldsymbol{v}_{2}^{T} \boldsymbol{h}_{2} \operatorname{sign}(\boldsymbol{\xi}_{2})$$

$$- \boldsymbol{\xi}_{1}^{T} \boldsymbol{h}_{1} \operatorname{sign}(\boldsymbol{\xi}_{1}) - \boldsymbol{\xi}_{2}^{T} \boldsymbol{h}_{2} \operatorname{sign}(\boldsymbol{\xi}_{2}).$$
(47)

By Young's inequality, the following relationships hold:

$$p\sum_{i=1}^{n} \tilde{\boldsymbol{W}}_{i}^{T} \hat{\boldsymbol{W}}_{i} \leq -\frac{p}{2} \sum_{i=1}^{n} \tilde{\boldsymbol{W}}_{i}^{T} \tilde{\boldsymbol{W}}_{i} + \frac{p}{2} \sum_{i=1}^{n} \|\boldsymbol{W}_{i}^{*}\|^{2}$$
(48)

$$\mathbf{v}_2^T \boldsymbol{\varepsilon} \le \frac{1}{2} \mathbf{v}_2^T \mathbf{v}_2 + \frac{1}{2} \boldsymbol{\varepsilon}^T \boldsymbol{\varepsilon} \le \frac{1}{2} \mathbf{v}_2^T \mathbf{v}_2 + \frac{1}{2} \bar{\varepsilon}^2$$
 (49)

$$\boldsymbol{\xi}_{1}^{T} \boldsymbol{\varpi}_{1} \boldsymbol{\xi}_{2} \leq \frac{1}{2} \boldsymbol{\xi}_{1}^{T} \boldsymbol{\varpi}_{1} \boldsymbol{\xi}_{1} + \frac{1}{2} \boldsymbol{\xi}_{2}^{T} \boldsymbol{\varpi}_{1} \boldsymbol{\xi}_{2}$$
 (50)

$$\boldsymbol{\xi}_1^T \boldsymbol{\varpi}_1 \boldsymbol{o}_1 \le \frac{1}{2} \boldsymbol{\xi}_1^T \boldsymbol{\varpi}_1 \boldsymbol{\xi}_1 + \frac{1}{2} \boldsymbol{o}_1^T \boldsymbol{\varpi}_1 \boldsymbol{o}_1$$
 (51)

$$v_1^T \boldsymbol{h}_1 \operatorname{sign}(\boldsymbol{\xi}_1) \le \frac{1}{2} v_1^T v_1 + \frac{1}{2} \|\boldsymbol{h}_1\|^2$$
 (52)

$$v_2^T h_2 \operatorname{sign}(\xi_2) \le \frac{1}{2} v_2^T v_2 + \frac{1}{2} ||h_2||^2$$
 (53)

$$-\boldsymbol{\xi}_{1}^{T}\boldsymbol{h}_{1}\operatorname{sign}(\boldsymbol{\xi}_{1}) \leq \frac{1}{2}\boldsymbol{\xi}_{1}^{T}\boldsymbol{\xi}_{1} + \frac{1}{2}\|\boldsymbol{h}_{1}\|^{2}$$
 (54)

$$-\boldsymbol{\xi}_{2}^{T}\boldsymbol{h}_{2}\operatorname{sign}(\boldsymbol{\xi}_{2}) \leq \frac{1}{2}\boldsymbol{\xi}_{2}^{T}\boldsymbol{\xi}_{2} + \frac{1}{2}\|\boldsymbol{h}_{2}\|^{2}.$$
 (55)

Substituting (48)–(55) into (47) gives

$$\dot{V} \leq -v_{1}^{T} \left(\mathbf{k}_{1} - \frac{1}{2} \mathbf{I} \right) v_{1} - v_{2}^{T} \left(\mathbf{k}_{2} - \frac{1}{2} \mathbf{I} \right) v_{2}
- \left(\mathbf{q}_{d} - \mathbf{q} \right)^{T} \mathbf{K}_{h} \left(\mathbf{q}_{d} - \mathbf{q} \right) - \frac{p}{2} \sum_{i=1}^{n} \tilde{\mathbf{W}}_{i}^{T} \tilde{\mathbf{W}}_{i}
- \xi_{1}^{T} \left(\mathbf{k}_{1} - \frac{(2\boldsymbol{\varpi}_{1} + \mathbf{I})}{2} \right) \xi_{1} - \xi_{2}^{T} \left(\mathbf{k}_{2} - \frac{(\boldsymbol{\varpi}_{1} + \mathbf{I})}{2} \right) \xi_{2}
+ \frac{p}{2} \sum_{i=1}^{n} \left\| \mathbf{W}_{i}^{*} \right\|^{2} + \frac{\tilde{\varepsilon}^{2}}{2} + \frac{\boldsymbol{o}_{1}^{T} \boldsymbol{\varpi}_{1} \boldsymbol{o}_{1}}{2} + \left\| \boldsymbol{h}_{1} \right\|^{2} + \left\| \boldsymbol{h}_{2} \right\|^{2}
\leq -\sigma V + \beta$$
(56)

where

$$\sigma = \min \begin{cases} \min_{\substack{i=1,\dots,n\\ i=1,\dots,n\\ \min_{i=1,\dots,n}}} (2k_{1i}-1), \\ \min_{\substack{i=1,\dots,n\\ i=1,\dots,n\\ \min_{i=1,\dots,n}}} (p/\lambda_{\max}(\boldsymbol{Q}_{i}^{-1})), \\ \min_{\substack{i=1,\dots,n\\ i=1,\dots,n\\ i=1,\dots,n}} (2k_{1i}-2\varpi_{1i}-1), \\ \min_{\substack{i=1,\dots,n\\ i=1,\dots,n}} (2k_{2i}-\varpi_{1i}-1) \end{cases}$$
(57)

$$\beta = \frac{p}{2} \sum_{i=1}^{n} \| \mathbf{W}_{i}^{*} \|^{2} + \frac{\bar{\varepsilon}^{2}}{2} + \frac{\mathbf{o}_{1}^{T} \mathbf{w}_{1} \mathbf{o}_{1}}{2} + \| \mathbf{h}_{1} \|^{2} + \| \mathbf{h}_{2} \|^{2}.$$

Further, (56) is multiplied by $e^{\sigma t}$, yields

$$\frac{d}{dt}(Ve^{\sigma t}) \le \beta e^{\sigma t}. (59)$$

(58)

By integrating (59), we can get

$$0 \le V \le \left(V(0) - \frac{\beta}{\sigma}\right) e^{-\sigma t} + \frac{\beta}{\sigma}.\tag{60}$$

Therefore, with appropriate constants σ and β , it is established that $V(t) \in \ell_{\infty}$. Consequently, the boundedness of v_1 , v_2 , ξ_1 , ξ_2 , q_d , and \tilde{W} is ensured. As a result, z_1 , z_2 , and \hat{W} are also confirmed to be bounded. The boundedness of the virtual controller α follows from (30) and the boundedness of z_1 . Moreover, from (24) and (26), we can conclude that all the states q and \dot{q} are bounded. Finally, the boundedness of τ is verified based on (36).

The proof of Theorem 1 is completed.

REFERENCES

- P. E. Dupont et al., "A decade retrospective of medical robotics research from 2010 to 2020," Sci. Robot., vol. 6, no. 60, 2021, Art. no. eabi8017.
- [2] X. Ke et al., "Review on robot-assisted polishing: Status and future trends," *Robot. Comput.-Integr. Manuf.*, vol. 80, Apr. 2023, Art. no. 102482.
- [3] L. Lestingi, D. Zerla, M. M. Bersani, and M. Rossi, "Specification, stochastic modeling and analysis of interactive service robotic applications," *Robot. Auton. Syst.*, vol. 163, May 2023, Art. no. 104387.
- [4] C. Véronneau et al., "Multifunctional remotely actuated 3-DOF supernumerary robotic arm based on magnetorheological clutches and hydrostatic transmission lines," *IEEE Robot. Autom. Lett.*, vol. 5, no. 2, pp. 2546–2553, Apr. 2020.
- [5] J. Luo, C. Zhang, W. Si, Y. Jiang, C. Yang, and C. Zeng, "A physical human–robot interaction framework for trajectory adaptation based on human motion prediction and adaptive impedance control," *IEEE Trans. Autom. Sci. Eng.*, vol. 22, pp. 5072–5083, 2024.
- [6] Z. Jin, W. Si, A. Liu, W.-A. Zhang, L. Yu, and C. Yang, "Learning a flexible neural energy function with a unique minimum for globally stable and accurate demonstration learning," *IEEE Trans. Robot.*, vol. 39, no. 6, pp. 4520–4538, Dec. 2023.
- [7] G. Li, Z. Li, C.-Y. Su, and T. Xu, "Active human-following control of an exoskeleton robot with body weight support," *IEEE Trans. Cybern.*, vol. 53, no. 11, pp. 7367–7379, Nov. 2023.
- [8] Z. Lu, W. Si, N. Wang, and C. Yang, "Dynamic movement primitives-based human action prediction and shared control for bilateral robot teleoperation," *IEEE Trans. Ind. Electron.*, vol. 71, no. 12, pp. 16654–16663, Dec. 2024.
- [9] Y. Maeda, T. Hara, and T. Arai, "Human–robot cooperative manipulation with motion estimation," in *Proc. IEEE/RSJ Int. Conf. Intell. Robots Syst.* Societal Role Robot. Next Millennium, vol. 4, 2001, pp. 2240–2245.
- [10] M. Gao, J. Oberländer, T. Schamm, and J. M. Zöllner, "Contextual task-aware shared autonomy for assistive mobile robot teleoperation," in *Proc. IEEE/RSJ Int. Conf. Intell. Robots Syst.*, 2014, pp. 3311–3318.
- [11] X. Yu, S. Liu, W. He, Y. Wu, H. Zhang, and Y. Wang, "A hybrid visual-haptic framework for motion synchronization in human-robot cotransporting: A human motion prediction method," *IEEE Robot. Autom. Mag.*, vol. 29, no. 4, pp. 25–35, Dec. 2022.
- [12] Y. Li and S. S. Ge, "Human-robot collaboration based on motion intention estimation," *IEEE/ASME Trans. Mechatronics*, vol. 19, no. 3, pp. 1007–1014, Jun. 2014.
 [13] X. Yu et al., "Bayesian estimation of human impedance and motion
- [13] X. Yu et al., "Bayesian estimation of human impedance and motion intention for human–robot collaboration," *IEEE Trans. Cybern.*, vol. 51, no. 4, pp. 1822–1834, Apr. 2021.
- [14] Z. Li, T. Zhang, P. Huang, and G. Li, "Human-in-the-loop cooperative control of a walking exoskeleton for following time-variable human intention," *IEEE Trans. Cybern.*, vol. 54, no. 4, pp. 2142–2154, Apr. 2024.

- [15] Z. Li, H. Wei, H. Zhang, and C. Liu, "A variable admittance control strategy for stable and compliant human–robot physical interaction," *IEEE Robot. Autom. Lett.*, vol. 10, no. 2, pp. 1138–1145, Feb. 2025.
- [16] F. Ferraguti, C. T. Landi, L. Sabattini, M. Bonfe, C. Fantuzzi, and C. Secchi, "A variable admittance control strategy for stable physical human-robot interaction," *Int. J. Robot. Res.*, vol. 38, no. 6, pp. 747–765, 2019.
- [17] A. Q. Keemink, H. Van der Kooij, and A. H. Stienen, "Admittance control for physical human–robot interaction," *Int. J. Robot. Res.*, vol. 37, no. 11, pp. 1421–1444, 2018.
- [18] Y. Chen et al., "Physical human-robot interaction based on adaptive impedance control for robotic-assisted total hip arthroplasty," IEEE/ASME Trans. Mechatronics, vol. 29, no. 6, pp. 4674–4686, Dec. 2024.
- [19] X. Xing, E. Burdet, W. Si, C. Yang, and Y. Li, "Impedance learning for human-guided robots in contact with unknown environments," *IEEE Trans. Robot.*, vol. 39, no. 5, pp. 3705–3721, Oct. 2023.
- [20] C. Zeng, H. Su, Y. Li, J. Guo, and C. Yang, "An approach for robotic leaning inspired by biomimetic adaptive control," *IEEE Trans. Ind. Informat.*, vol. 18, no. 3, pp. 1479–1488, Mar. 2022.
- [21] H.-Y. Li et al., "Stable and compliant motion of physical humanrobot interaction coupled with a moving environment using variable admittance and adaptive control," *IEEE Robot. Autom. Lett.*, vol. 3, no. 3, pp. 2493–2500, Jul. 2018.
- [22] M. Mujica, M. Crespo, M. Benoussaad, S. Junco, and J.-Y. Fourquet, "Robust variable admittance control for human–robot co-manipulation of objects with unknown load," *Robot. Comput. Integr. Manuf.*, vol. 79, Feb. 2023, Art. no. 102408.
- [23] A. Ajoudani, C. Fang, N. Tsagarakis, and A. Bicchi, "Reduced-complexity representation of the human arm active endpoint stiffness for supervisory control of remote manipulation," *Int. J. Robot. Res.*, vol. 37, no. 1, pp. 155–167, 2018.
- [24] C. Liu, G. Peng, Y. Xia, J. Li, and C. Yang, "Robot skill learning system of multi-space fusion based on dynamic movement primitives and adaptive neural network control," *Neurocomputing*, vol. 574, Mar. 2024, Art. no. 127248.
- [25] C. Zeng, C. Yang, H. Cheng, Y. Li, and S.-L. Dai, "Simultaneously encoding movement and sEMG-based stiffness for robotic skill learning," *IEEE Trans. Ind. Informat.*, vol. 17, no. 2, pp. 1244–1252, Feb. 2021
- [26] X. Mengying, Y. Xiaoli, X. Chenli, and Y. Bin, "EMG signal processing and application based on empirical mode decomposition," *Math. Comput. Sci.*, vol. 9, no. 1, pp. 99–103, 2019.
- [27] L. Liu, P. Liu, E. A. Clancy, E. Scheme, and K. B. Englehart, "Signal whitening preprocessing for improved classification accuracies in myoelectric control," in *Proc. IEEE 37th Annu. Northeast Bioeng. Conf. (NEBEC)*, 2011, pp. 1–2.
- [28] Y. Zheng and X. Hu, "Interference removal from electromyography based on independent component analysis," *IEEE Trans. Neural Syst. Rehabil. Eng.*, vol. 27, no. 5, pp. 887–894, May 2019.
- [29] L. Bi et al., "A review on EMG-based motor intention prediction of continuous human upper limb motion for human-robot collaboration," *Biomed. Signal Process. Control*, vol. 51, pp. 113–127, May 2019.
- [30] Q. Wu, Z. Wang, Y. Chen, and H. Wu, "Barrier Lyapunov function-based fuzzy adaptive admittance control of an upper limb exoskeleton using RBFNN compensation," *IEEE/ASME Trans. Mechatronics*, vol. 30, no. 1, pp. 3–14, Feb. 2025.
- [31] X. Yu, B. Li, W. He, Y. Feng, L. Cheng, and C. Silvestre, "Adaptive-constrained impedance control for human-robot co-transportation," *IEEE Trans. Cybern.*, vol. 52, no. 12, pp. 13237–13249, Dec. 2022.
- [32] G. Peng, T. Li, C. Yang, and C. P. Chen, "Approximation-based admittance control of robot-environment interaction with guaranteed performance," *IEEE Trans. Syst., Man, Cybern., Syst.*, vol. 54, no. 10, pp. 6482–6494, Oct. 2024.
- [33] Y. Li, K. Yu, and S. Tong, "Adaptive backstepping control for multiple Euler-Lagrangian systems with independent dynamic communication," *Automatica*, vol. 160, Feb. 2024, Art. no. 11143.
- [34] G. Wang, "Distributed control of higher-order nonlinear multi-agent systems with unknown non-identical control directions under general directed graphs," *Automatica*, vol. 110, Dec. 2019, Art. no. 108559.
- [35] Y. Li, Y.-X. Li, and S. Tong, "Event-based finite-time control for nonlinear multiagent systems with asymptotic tracking," *IEEE Trans. Autom. Control*, vol. 68, no. 6, pp. 3790–3797, Jun. 2023.
- [36] K. Zhao, L. Chen, W. Meng, and L. Zhao, "Unified mapping function-based neuroadaptive control of constrained uncertain robotic systems," *IEEE Trans. Cybern.*, vol. 53, no. 6, pp. 3665–3674, Jun. 2023.

- [37] G. Peng, C. Yang, and C. P. Chen, "Neural control for human–robot interaction with human motion intention estimation," *IEEE Trans. Ind. Electron.*, vol. 71, no. 12, pp. 16317–16326, Dec. 2024.
- [38] C. Yang, D. Huang, W. He, and L. Cheng, "Neural control of robot manipulators with trajectory tracking constraints and input saturation," *IEEE Trans. Neural Netw. Learn. Syst.*, vol. 32, no. 9, pp. 4231–4242, Dec. 2024.
- [39] B. Xu, Y. Fan, and S. Zhang, "Minimal-learning-parameter technique based adaptive neural control of hypersonic flight dynamics without back-stepping," *Neurocomputing*, vol. 164, pp. 201–209, Sep. 2015.
- [40] Y. Wu, M. Chen, H. Li, and M. Chadli, "Event-triggered-based adaptive NN cooperative control of six-rotor UAVs with finite-time prescribed performance," *IEEE Trans. Autom. Sci. Eng.*, vol. 21, no. 2, pp. 1867–1877, Apr. 2024.
- [41] H. Ma, Q. Zhou, H. Li, and R. Lu, "Adaptive prescribed performance control of a flexible-joint robotic manipulator with dynamic uncertainties," *IEEE Trans. Cybern.*, vol. 52, no. 12, pp. 12905–12915, Dec. 2022
- [42] P. Yang and Y. Su, "Proximate fixed-time prescribed performance tracking control of uncertain robot manipulators," *IEEE/ASME Trans. Mechatronics*, vol. 27, no. 5, pp. 3275–3285, Oct. 2022.
- [43] Y. Xia, K. Xiao, and Z. Geng, "Event-based adaptive fuzzy control for stochastic nonlinear systems with prescribed performance," *Chaos Solitons Fractals*, vol. 180, Mar. 2024, Art. no. 114501.
- [44] L. Li, Z. Liu, S. Guo, Z. Ma, and P. Huang, "Adaptive practical predefined-time control for uncertain teleoperation systems with input saturation and output error constraints," *IEEE Trans. Ind. Electron.*, vol. 71, no. 2, pp. 1842–1852, Feb. 2024.

- [45] Y. Yang et al., "Adaptive predefined time control for stochastic switched nonlinear systems with full-state error constraints and input quantization," *IEEE Trans. Cybern.*, early access, Mar. 10, 2025, doi: 10.1109/TCYB.2025.3531381.
- [46] K. Zhao, Y. Song, C. P. Chen, and L. Chen, "Adaptive asymptotic tracking with global performance for nonlinear systems with unknown control directions," *IEEE Trans. Autom. Control*, vol. 67, no. 3, pp. 1566–1573, Mar. 2022.
- [47] K. Zhao, F. L. Lewis, and L. Zhao, "Unifying performance specifications in tracking control of MIMO nonlinear systems with actuation faults," *Automatica*, vol. 155, Sep. 2023, Art. no. 111102.
- [48] Y. Fan, C. Yang, B. Li, and Y. Li, "Neuro-adaptive-based fixed-time composite learning control for manipulators with given transient performance," *IEEE Trans. Cybern.*, vol. 54, no. 12, pp. 7668–7680, Dec. 2024.
- [49] J. Luo, D. Huang, Y. Li, and C. Yang, "Trajectory online adaption based on human motion prediction for teleoperation," *IEEE Trans. Autom. Sci. Eng.*, vol. 19, no. 4, pp. 3184–3191, Oct. 2022.
- [50] Y. Xia et al., "Stochastic neural network control for stochastic nonlinear systems with quadratic local asymmetric prescribed performance," *IEEE Trans. Cybern.*, vol. 55, no. 2, pp. 867–879, Feb. 2025.
- [51] L. Sciavicco and B. Siciliano, "A solution algorithm to the inverse kinematic problem for redundant manipulators," *IEEE J. Robot. Autom.*, vol. 4, no. 4, pp. 403–410, Aug. 1988.
- [52] E. Burdet, D. W. Franklin, and T. E. Milner, Human Robotics: Neuromechanics and Motor Control. Cambridge, MA, USA: MIT Press, 2013.
- [53] A. Levant, "Higher-order sliding modes, differentiation and output-feedback control," *Int. J. Control*, vol. 76, nos. 9–10, pp. 924–941, 2003.